Multi-sensor approach for high space and time resolution land surface temperature

Ankur R. Desai[1],*, Anam M. Khan[2], Ting Zheng[3], Sreenath Paleri[1], Brian Butterworth[1], Temple R. Lee[4], Joshua B. Fisher[5], Glynn Hulley[5], Tania Kleynhans[6], Aaron Gerace[6], Philip A. Townsend[3], Paul Stoy[7], Stefan Metzger[8,1]

1. Dept of Atmospheric and Oceanic Sciences, University of Wisconsin-Madison, 1225 W Dayton St, Madison, WI 53711 USA

2. Nelson Institute for Environmental Studies, University of Wisconsin, 550 North Park St, Madison, WI 53706 USA

3. Department of Forest and Wildlife Ecology, University of Wisconsin-Madison

1630 Linden Drive, Madison, WI, 53706 USA

4. Cooperative Institute for Mesoscale Meteorological Studies and NOAA Air Resources Laboratory Atmospheric Turbulence and Diffusion Division, 456 S. Illinois Ave, Oak Ridge, TN 37830 USA

5. Jet Propulsion Laboratory, California Institute of Technology, 4800 Oak Grove Dr., Pasadena, CA, 91109

6. Chester F. Carlson Center for Imaging Science, Rochester Institute of Technology, 54 Lomb Memorial Drive Rochester, NY 14623

7. Department of Biological Systems Engineering, University of Wisconsin – Madison, 460 Henry Mall, Madison, WI 53706, USA

8. Battelle, National Ecological Observatory Network. 1685 38th Street, Boulder, CO 80301, USA

* Corresponding author: Ankur R Desai, Dept of Atmospheric and Oceanic Sciences, University of Wisconsin-Madison, 1225 W Dayton St, Madison, WI 53706 USA, +1-608-520-0305, desai@aos.wisc.edu, ORCID ID: 0000-0002-5226-6041, http://flux.aos.wisc.edu

Key Points:

- Fusion of satellites with models for high space and time resolution land surface temperature needed for many surface-atmosphere studies
- Developed an approach that evaluates well across array of towers and aircraft observations from an intensive field experiment
- Additional downscaling with airborne hyperspectral imagery further refines identification of hot spots as seen in drone observations

Abstract

Surface-atmosphere fluxes and their drivers vary across space and time. A growing area of interest is in downscaling, localizing, and/or resolving sub-grid scale energy, water, and carbon fluxes and drivers. Existing downscaling methods require inputs of land surface properties at relatively high spatial (e.g., sub-kilometer) and temporal (e.g., hourly) resolutions, but many observed land surface drivers are not available at these resolutions. We evaluate an approach to overcome this challenge for land surface temperature (LST), a World Meteorological Organization Essential Climate Variable and a key driver for surface heat fluxes. The Chequamegon Heterogenous Ecosystem Energy-balance Study Enabled by a High-density Extensive Array of Detectors (CHEESEHEAD19) field experiment provided a scalable testbed. We downscaled LST from satellites (GOES-16 and ECOSTRESS) with further refinement using airborne hyperspectral imagery. Temporally and spatially downscaled LST compared well to observations from a network of 20 micrometeorological towers and airborne in addition to Landsat-based LST retrieval and drone-based LST observed at one tower site. The downscaled 50-meter hourly LST showed good relationships with tower (r^2=0.79, precision=3.5 K) and airborne (r^2=0.75, precision=2.4 K) observations over space and time, with precision lower over wetlands and lakes, and some improvement for capturing spatio-temporal variation compared to geostationary satellite. Further downscaling to 10 m using hyperspectral imagery resolved hotspots and cool spots on the landscape detected in drone LST, with significant improvement in precision by 1.3 K. These results demonstrate a simple pathway for multi-sensor retrieval of high space and time resolution LST.

Plain Language Summary

The temperature of Earth's surface over land – land surface temperature (LST) – is an important variable to observe and forecast. Variation in LST over space and time at scales of meters and hours influence processes in the atmosphere, soils, vegetation, and water. For worldwide coverage of LST, we rely on Earth-observing satellites. However, there are challenges in how finely LST can be observed over space versus how often LST can be observed over time, given the characteristics of any one satellite's orbit, not to mention the obscuring effect of clouds. Therefore, methods are needed that combine multiple satellites if we want to observe LST at high space and time resolution. Here, we develop such an approach and test its accuracy over a testbed of extensive LST observations made by towers, drones, and aircraft during a field experiment in Northern Wisconsin USA.

Keywords: Land-surface temperature, remote sensing, CHEESEHEAD19, ECOSTRESS, GOES

Index terms: 480 Remote sensing; 1910 Data assimilation, integration and fusion; 3322 Land/Atmosphere interactions; 1980 Spatial analysis and representation

1. Introduction

Land surface temperature (LST) is a World Meteorological Organization Essential Climate Variable that links the thermodynamics of earth's land surface with the dynamics of the overlying atmosphere (Berlward, 2016; Dirmeyer *et al*., 2012). LST, equivalent to surface skin temperature, refers to the apparent temperature of an infinitesimally thin surface of ground (English, 2008). It is a consequence of the difference in the net radiative energy budget of the surface and rate of heat conduction into the ground. LST can vary greatly over short distances (Yi *et al*., 2020), as anyone who has walked across wet and dry sand on a beach during a sunny summer day can attest. For LST observation systems, then, the challenge becomes how to integrate that variation at space and time scales relevant to land-atmosphere interactions.

LST is most commonly measured based on principles related to radiative observations made across various wavelengths in the thermal infrared spectrum, given the tight relationship of electromagnetic blackbody radiation to temperature, as provided by the Planck function and in integrated form to the Stefan-Boltzmann relationship. The peak of earth's outgoing surface longwave radiation is in this region and thermal infrared brightness temperatures reflect surface temperatures integrated over a few micrometers, making it a good proxy for LST (Hulley and Ghent, 2019). After calculation of emissivity, these observations allow for inversion of LST from longwave radiation measurements (Wang *et al*., 2014). On a fixed or moving platform, thermopile sensors facing earth can measure longwave radiation and be used to calculate *in situ* LST, after accounting for atmospheric correction. Typically, LST observations on a fixed grid are derived from thermal infrared brightness temperature or outgoing longwave radiation observations made by earth-observing satellites, in polar, irregular, or geostationary orbits (English, 2008; Scarino *et al*., 2013; Li *et al*., 2013). Orbits, costs, and logistics lead to tradeoffs retrieving high time frequency (typically from geostationary orbits) versus high spatial resolution (typical from polar or irregular orbits). Additionally, satellite LST is not easily retrieved in areas under heavy cloud cover.

Continuous high time and space resolution LST, including the diel cycle, is of high value for a number of scientific investigations (e.g., Kröninger *et al*., 2019). LST can vary by tens of degrees K over meters and change within seconds to hours, for example due to shadows, wind, passing of clouds (Yi *et al*., 2020), or irrigation. These changes in LST then influence the heating of the soil, vegetation, and atmosphere over the course of the day (Dirmeyer *et al*., 2013; Taylor *et al*., 2012), and the dynamics that ensue as a result. In many land surface models, for example those used in numerical weather prediction, LST is usually a derived value inferred from the modeled surface energy balance and soil physics, often averaged over an entire grid cell or a land cover tile, and not resolved at scales below hundreds of meters. Continuous LST over scales of meters and hours would provide a valuable benchmark to evaluating atmospheric surface layer and soil heat diffusion parameterizations, estimating turbulent heat fluxes (Xu *et al*., 2018), assimilation of LST for model grids (Bosilovich *et al*., 2007; Zheng *et al*., 2012), scaling of land-atmosphere fluxes and feedbacks (Metzger, 2018; Xu *et al*., 2018), and answering science questions related to fine-scale sub-kilometer space and sub-daily time heterogeneity of landscapes and habitats (Guillevic *et al*., 2019; Pincebourde *et al*., 2020). Biological organisms, in particular, are strongly influenced by small-scale microclimates and scaling these responses across regions is nonlinear (Bütikoger *et al*., 2020).

Given these needs, fusion approaches have been designed to combine multiple satellite data products and increase their joint space, time, and clear sky coverage (Anderson *et al*., 2021; Gao *et al*., 2012; Hu *et al*., 2020; Liu *et al*., 2006). However, current and upcoming generation satellites and computational capacity provide an even richer array of data fusion options (Freitas *et al*., 2013; Khan *et al*., 2021; Tomlinson *et al*., 2011). For example, NASA's ECOsystem Spaceborne Thermal Radiometer Experiment on Space Station (ECOSTRESS) is a thermal imager on the International Space Station (ISS) that, from this relatively low (~400 km) and fast precessing orbit, can image the globe at roughly 1-5 day repeat (at different hours of day every orbit) and at 70-m resolution (Fisher *et al*., 2020). Meanwhile, the latest NOAA Geostationary Operational Environmental Satellites (GOES-16 and GOES-17) image the Western Hemisphere at a nominal 15-minute timestep with approximately 2 km resolution depending on view geometry. Fusion of these products have not been evaluated. High space and time resolution LST has been attempted in some locations (e.g., Sismanidis *et a*l., 2016a,b, 2018), but there is a need for greater evaluation across multiple approaches and sensors.

A number of remotely sensed features beyond thermal infrared also relate to LST and could improve downscaling (Yue *et al*., 2020). For example, observations in visible and microwave wavelengths relate to processes such as vegetation activity and soil moisture, respectively, that in turn relate to fine-scale variation in LST. Hyperspectral remote sensing (*aka* imaging spectroscopy), in particular, may allow for fine-tuning of LST by linking to surface mineralogy and crown-level foliar functional characteristics that affect foliar thermodynamics.

Prior studies often lacked a comprehensive spatial and temporal database of *in situ* LST at relevant space and time scales for evaluating LST fusion products and their uncertainty, critical for model assimilation (Freitas *et al*., 2010; Bosilovich *et al*., 2007). The recent Chequamegon Heterogeneous Ecosystem Energy-balance Study Enabled by a High-density Extensive Array of Detectors (CHEESEHEAD19) (Butterworth *et al*., 2021) field campaign included an array of towers, drones, and aircraft, in addition to custom remote sensing thermal imagery from Landsat-8 (Gerace *et al*., 2020) that provides a comprehensive, open-access testbed for any fusion approach. Radiometric-derived LST over various landscapes is available over a four-month period across a nearly 1000 km^2 area of a heterogenous, flat landscape of northern Wisconsin USA. Furthermore, visible and near infrared hyperspectral airborne imagery at 1 m resolution was flown in the domain several times, providing a second data source to evaluate alternative downscaling and fusion approaches based on surface cover characteristics rather than emissivity.

Here, we evaluate a novel high space (50 m and 10 m) and time (hourly) resolution LST fusion approach using next generation thermal imagery. We ask: how reliably can we fuse high space and high temporal resolution satellites to generate continuous, cloud-free gridded LST? Further, hyper-resolution drone LST imagery at the sub-meter scale allows us to further evaluate downscaling of this gridded product to even smaller domains, necessary for some scientific applications (Pincebourde *et al*., 2020). Thus, within a subset of our study area, we also test whether we can further downscale to higher resolution by connecting hyperspectral indices combined with the LST fusion. Finally, we discuss the implication of the work for advancing land-atmosphere interaction science.

2. Materials and Methods

Our general approach employs hierarchical fusion (Fig. 1). As a prior, cloud-free, coarse-resolution (12 km) estimate of LST, we used data-assimilation constrained hourly LST from a set of three land surface models. These modelled LSTs are then fit on a pixel level to gap-fill geostationary satellite LST to generate gap-free medium resolution (1-2 km) hourly LST. Further spatial downscaling is accomplished using the suite of cloud-screened, quality-controlled high-resolution (50 m) LST and generating a regression surface that links the medium and high-resolution LST across all collected time points. The resulting high space and time resolution LST grids are then evaluated against a range of independent tower, aircraft, and satellite estimates of LST. Finally, an additional ultra-high resolution downscaling to 10 m is conducted using hyperspectral imagery over an area where coincident ultra-high resolution drone LST were also measured.

2.1 Site description

Analyses are centered on the observations collected during the CHEESEHEAD19 field campaign (Butterworth *et al*., 2021) conducted near Park Falls, Wisconsin USA in central region of the North American continent from June to October 2019. CHEESEHEAD19 was an intensive surface-atmosphere field experiment investigating the role of surface spatial heterogeneity on atmospheric dynamics and the surface energy balance. As a result, a suite of observations was collected over a 10 km × 10 km core domain and a 30 km × 30 km extended domain, centered on the WLEF Park Falls Ameriflux very tall eddy covariance (US-PFa) tower, which is also a NOAA greenhouse gas (LEF) tall tower. Observations included 20 micrometeorology towers within the core domain, ground-based atmospheric profiling, drone and airborne remote sensing at various locations throughout, and more than 10,000 km of low-level meteorological aircraft observations in the extended domain. Upwelling and downwelling longwave radiation observations from towers, IR skin temperature retrieved from aircraft, and an independent satellite LST estimate from Landsat were used here to evaluate the LST product.

2.2 Input data

All data products used for the generation of high (50 m) and ultra-high (10 m) resolution LST were acquired from public open-access data repositories (Table 1). Each data product was extracted for all acquisitions from 1 June to 31 October ,2019 and subset to a domain that encompassed the CHEESEHEAD19 extended domain (Fig. 1). Descriptions of each data product are provided here.

For the prior modeled LST, we acquired LST from the National Land Data Assimilation System version 2 (NLDAS-2) (Xia *et al*., 2012). NLDAS is an observation reanalysis that constructs an optimal meteorological driver forcing based on gauge precipitation and bias-corrected shortwave radiation. This forcing is provided to a suite of land surface models, which output a common set of responses, including LST. NLDAS products are provided on a ⅛ degree grid (approximately 12.5 km) across North America at hourly timestep. We extracted LST for the three land surface models that are part of NLDAS and output surface skin temperature: Mosaic (Koster and Saurez,

1992), Noah-2.8 (Chen *et al*., 1996), and VIC (Liang *et al*., 1994). We calculated mean and variance moments on the modeled LST as a prior.

NOAA's Geostationary Operational Environmental Satellites (GOES) are the primary U.S. operational geostationary weather satellites in orbit over the Western Hemisphere (Schmit *et al*., 2017). In recent years, LST has become a primary operational product of the GOES-R Advanced Baseline Imager (ABI) in the current generation GOES-16 and GOES-17 satellites (Yu *et al*., 2009). These outputs, at an approximately 2 km spatial resolution, are produced based on thermal channel split-window retrieval using the 11.2 um and 12.3 um channels with high surface emission and low atmospheric absorption. The algorithm also uses prescribed surface emissivity and an atmospheric radiative transfer model to produce an output at least once an hour for the Northern Hemisphere (more fully described at: https://www.goes-r.gov/products/baseline-LST.html). Target accuracy is 2.5 K and evaluations have shown it to be approaching 1.5 K (Yu *et al*., 2012).

ECOsystem Spaceborne Thermal Radiometer Experiment on Space Station (ECOSTRESS) is a thermal imager flown on the International Space Station (ISS) (Fisher *et al*., 2020; Hulley *et al*., 2017). ECOSTRESS was launched in June 2018 and has been providing harmonized Level 2 70 × 70 m data products on surface temperature, evapotranspiration, water use efficiency, and drought stress since launch. We acquired the Level 2 Land Surface Temperature and Emissivity product and the ECOSTRESS cloud cover product (described at https://lpdaac.usgs.gov/documents/423/ECO2_User_Guide_V1.pdf). LST is derived from a physically-based Temperature and Emissivity Separation (TES) algorithm (Gillespie *et al*. 1998; Hulley and Hook 2011). Atmospheric correction is performed using the RTTOV radiative transfer model (Matricardi 2008; Saunders *et al*. 1999). Retrieval is based on thermal radiances in the 8.29 um, 8.78 um, 9.20 um, 10.49 um, and 12.09 um bands. Validation accuracy was reported as 1.07 K (Hulley *et al.*, in press). QA flags were used to limit to best or nominal quality observations. The ECOSTRESS Level-2 CLD cloud-mask (https://lpdaac.usgs.gov/products/eco2cldv001/) was applied to mask any cloud contaminated pixels. The ISS orbit is not sun-synchronous, so scenes are retrieved at different times of day, with a repeat interval of 1-5 days depending on location. A total of 118 full domain scenes were retrieved over the CHEESEHEAD19 domain during the study period spanning all hours of the day. Of these, 49 images were at least 50% cloud free. From that subset, 25 images (~weekly) were retained that were significantly ($p<0.001$) correlated ($r>0.3$) with the GOES imagery and had <50% cloud cover.

The University of Wisconsin hyperspectral imager is a visible to near-infrared (400-2500 nm) imaging spectrometer designed for airborne applications (HySpex, Norsk Elektro Optikk, Oslo, Norway). The HySpex consists of two boresighted imagers measuring a total of 474 narrow bands between 400-1000 nm (3.26 nm spectral resolution) and 930-2500 nm (5.45 nm spectral resolution). In CHEESEHEAD19, the HySpex was flown on a State of Wisconsin Department of Transportation Cessna 210 at 1,400 m altitude above ground, allowing for a nominal 1 m pixel size over the core domain. The HySpex was flown multiple times over the study period (26 June through 30 August). The CHEESEHEAD19 study area is covered by 21 flightlines flown +/- 2 hr around solar noon. Here, observations from dates closest to the date of the drone overflight were used. Images were orthorectified (following Schlapfer and Richter 2002) and

atmospherically corrected (following Adler-Golden *et al*. 1999) to surface reflectance using LibRadTran (Emde *et al*. 2016) open-source code by Liu *et al*. (2019). Flightlines were subset to the regions of drone overflights. In our analyses, we used a normalized spectral index approach that reduced the need for additional processing to reduce bidirectional reflectance variation.

2.3 Evaluating LST data

Several data products were used to evaluate the 50 m and 10 m downscaled LST. These are noted in Table 2 and briefly described here. The University of Wyoming King Air (UWKA) is a meteorological research aircraft that flew linear transects in CHEESEHEAD19 focused on eddy covariance applications during three 4-day periods within the experiment window (9-13 July 2019, 20-23 August 2019, 24-28 September 2019). Flights were flown in mid-morning and mid-afternoon, usually 15 legs at 100 m and 400 m altitude above ground spanning the 30 × 30 km extended domain, at approximately 90 m s^{-1}. UWKA included a downward-looking radiative thermometer (Heimann KT-19.85), which reports observed brightness temperature for the 9.5-11.5 um IR spectrum with 0.5 K accuracy and 0.2 K RMSE precision over 1 s (~90 m at flight speed). This instrument reported temperature at 100 m flight altitude above ground was compared to our LST fusion to evaluate spatial variability. UWKA geospatial coordinates were used to average all 100-m above ground flight leg LST observations overlapping each pixel.

Twenty eddy covariance flux towers were located in the 10 × 10 km inner domain. These towers were located in a range of ecosystems, including mixed forests, evergreen forests, wetlands, and grass fields. Seventeen of these had four-component net radiation measurements (Huskeflux NR01) available, from which upwelling and downwelling longwave radiation were extracted to calculate LST. Followed Malakar *et al*. (2018), we estimated surface emissivity at 10.6 μm and 11.3 μm based on the ASTER satellite global emissivity database, provided at 30 m resolution (Hulley *et al*., 2015). Surface emissivity was averaged over a 90 × 90 m box around the center coordinate of each tower. Hourly-averaged LST estimates for each tower were then used to compare to LST from the hourly fusion product.

Landsat 8 based LST was also acquired for this domain. Here, we acquired an enhanced LST product from Landsat based on the two-channel split window algorithm from Gerace *et al*. (2020), an improvement over the operational single-channel algorithm. Given the high cloud cover of most scenes during the intermittently and anomalously rainy CHEESEHEAD19 campaign, we focused on a single scene collected on 26 September 2019 as an evaluation LST whereas ECOSTRESS was used for training given its more frequent repeat coverage. Landsat LST thermal resolution is 100 m, but output at 30 m by cubic convolution to match the visible bands. We directly compared this LST to our downscaled 50 m LST, first re-upscaling the Landsat temperature data to 50 m.

The NOAA uncrewed airborne system drone is a DJI S-1000 that was outfitted with a downward-pointing FLIR Tau 2 infrared camera during CHEESEHEAD19, as well as iMet-XQ sensors to sample temperature, moisture, and pressure in situ. The infrared camera has a 7.5-mm lens, 336 × 256 pixel resolution, and view angle of 90° × 69° (Dumas *et al*. 2016, 2017; Lee *et al*. 2017, 2019). The DJI S-1000 was flown in July at a single eddy covariance flux tower site hourly throughout the day, over an area of approximately 500 m × 500 m, which was a distance

sufficient to cover a significant number of pixels. We focus on data obtained during the flights on 12 July; flights on the other days with the DJI S-1000 during the July campaign were smaller in radius and thus less useful for downscaling.

2.4 LST fusion methodology

We apply a fusion approach similar to the STARFM approach for downscaling of MODIS to Landsat resolution, based on pixel-level and neighborhood correlation (Gao *et al*., 2006; Gao *et al*., 2015). However, by virtue of having a large number of high-resolution images and the need to capture diel cycle of LST, the approach was modified to capture diel time variation. The basics are provided below and evaluated in the results.

The first step was to gap-fill cloud covered LST data in GOES, as indicated by the GOES cloud flag. To do so, we used the NLDAS LST estimate from each of the three models. The average and standard deviation are used here as a prior estimate of LST. For each GOES pixel, the relevant NLDAS pixel is geolocated using a nearest neighbor approach. A linear regression debias is then applied to the hourly NLDAS LST for the same hour in each day when GOES LST was observed, so that each 12.5 km NLDAS pixel would have ~40 independent regressions against each ~2 km GOES pixel. Regression was performed using the fitexy routine in the IDL Astronomy Library (Landsman, 1993), allowing the slope and intercept to account for errors in both the predictor variable X (uncertainty of GOES, nominally set to 1.5 K) and response variable in Y (standard deviation of NLDAS LST across the three models). For the 153-day period, each GOES pixel had 24 separate regressions (one for each hour of the day) applied to the matching NLDAS pixel. This enabled us to bias of mean and variance of LST over the season, and also correct for differences in the magnitude of the diel cycle. Missing values of LST in GOES were then replaced with these debiased NLDAS values.

Next, ECOSTRESS was used to downscale the gap-free 2 km GOES image to a standard 50 m grid. Both were first re-projected into a standard UTM grid with 50x50 m square pixels. For each ECOSTRESS pixel (for most points, up to 25 observations over the 153-day period, generally equally distributed across all hours of day and night), we extracted all nearest GOES observations matching in space and time. Linear slope and intercept were then calculated for each again using fitexy with the documented uncertainty of 1 K for ECOSTRESS. Slopes outside of the 98% confidence interval (0.9-1.4) of all calculated slopes were rejected to prevent unreasonable LST extrapolations. For the missing slope values, a neighborhood smoothing algorithm was applied from nearby pixels, and intercept recalculated based on regression of slope to intercept ($r=-0.24$). Unlike STARFM, which only uses 1 or 2 Landsat scenes to downscale MODIS, here we are using all ECOSTRESS images and all matching GOES images to develop a seasonal fit. This seasonal fit is then applied to the GOES gap-filled imagery to downscale the image to hourly, 50 m resolution LST.

For ultra-high resolution (10 m) downscaling test, additional covariates were brought from 1 m HySpex imagery. Data from three three HySpex flight acquisition scenes (26 June 2019, 11 July 2019, 8 August 2019) were chosen to bracket the acquired drone LST image on 12 July 2019. The drone LST and HySpex imagery were upscaled to 10 m resolution using simple averaging and coaligned to a common grid. This had the benefit of increasing the signal-to-noise in the

hyperspectral data. Following the approach by Dubois *et al*. (2018), analyses of the hyperspectral imagery utilized normalized difference spectral indices (NDSIs) with all two-band combinations of wavelengths:

$$NDSI(i,j) = (Band\_i - Band\_j) / (Band\_i + Band\_j) \qquad \text{(Equation 1)}$$

Statistically, this enables identification of key narrowband spectral features while the use of ratios greatly decreases cross-track illumination effects related to sun-target-sensor geometry (i.e., bidirectional reflectance distribution function, BRDF). The downscaled 50 m LST from ECOSTRESS was subtracted from the upscaled 10 m drone LST to produce an LST anomaly map. Each HySpex NDSI was separately regressed against the LST anomaly map. The highest R^2 band ratios consistent in all three HySpex dates were then selected to develop a linear model to predict fine-scale LST from the anomaly map and three selected HySpex bands, after which multiple linear regression was used to construct an ultra-high resolution 10 m LST. Use all of 474 bands in Hyspex allowed us to evaluate possible novel combinations of reflectance that could help explain variation in LST. Code that walks through the fusion methodology can be found at: https://github.com/DesaiLab/LSTfusion

3. Results

3.1 Cloud-free geostationary LST

After the diurnal regression step is applied, hourly NLDAS average LST corresponds well to retrieved GOES LST across the study domain (Fig. 2). Overall 82% of the variation of GOES LST can be explained by NLDAS-modeled LST, though a small domain wide cold bias of −0.78 K persists, with larger variance toward colder temperatures, potentially pointing to view-angle effects from shading or undetected clouds in GOES. Using the pixel-level, hour-specific regression, 60% of cloud-identified gaps were replaced with the modeled values. Missing observations were most prevalent late at night (9 UTC, 51% missing), during periods of fog or low-level stratus clouds, and a minimum in late afternoon (21 UTC, 25% missing), mostly during periods of extensive fair-weather cumulus cloud decks. Individual scenes had between 0-97% of pixels missing, averaging over 50% in early summer, during a particularly rainy period, to less than 40% during the normally drier autumn.

3.2 High-resolution fusion

Similar levels of correlation were found between the GOES gap-filled LST with retrieved ECOSTRESS LST (Fig. 3, see Fig. 1 for example of overlapping GOES and ECOSTRESS image), though with significant spatial variation. In general, within-pixel temporal correlation (r=0.59 to 0.95) was stronger than across-pixel spatial correlation (r=0.32 to 0.74). Low correlations were primarily found over water bodies, in particular the larger lake in the north of the domain, potentially from differences in retrieval algorithms or a documented cold bias on cooler surfaces in ECOSTRESS (Hulley *et al*., in press).

The regression of GOES to ECOSTRESS also varied in space, with median slope and intercept of 1.1 and −0.87 K, respectively (Fig. 3a and Fig. 3b). Particularly notable is the identification of urban areas (the City of Park Falls on western side) and highways. Slope and intercept were negatively correlated (r=−0.24). Locations with low slope (weaker diel and/or seasonal variation in ECOSTRESS compared to GOES) generally had higher (warmer) intercepts; for example, indicative of urban heat island or asphalt heat storage effects. Conversely, high slopes (stronger diel and/or seasonal variation) occurred in areas with lower (colder) intercepts, such as topographically low spots where cold-air pooling may depress mean temperature, including lakes, rivers, and bottomland forested areas.

These slopes and intercepts were applied to the GOES cloud-free LST to develop the downscaled high-resolution LST. Further evaluation of short time series of this product shows how the downscaled high-resolution LST better reflects differences in diurnal cycle and means from the coarser resolution NLDAS or GOES, and closer to the tower observed variations in LST, best resolved over wetlands (Fig. 4a), but also reflecting good correspondence at resolving the warmer nighttime temperatures over forests (Fig. 4a and 4b) and cooler daytime temperatures over lakes (Fig. 4d).

3.3 Evaluation

We evaluate downscaled LST against several estimates of LST from tower, aircraft, and satellite. Spatial patterns were well captured in the high-resolution LST as compared to aircraft LST (Fig. 5a, r^2=0.75) with small bias (−0.65 K) and a precision of 2.4 K. A larger > 5 K bias is apparent in high LST locations, where the fusion product smooths out extremes given its linear averaging approach. In contrast, seasonal temporal variation biases were found to be more prevalent with colder temperatures, where the downscaled LST tended to underestimate the coldest temperatures observed by the towers (Fig. 5b, r^2 = 0.79), though with better correlation. No significant difference was found in the LST time series variation across land cover type, whether deciduous forest, evergreen forest, or wetland, with general RMSE of 3.5 K. Bias was larger than the airborne data at −2.6 K, especially later into the fall. Correlations within a land cover type were higher (r^2~0.85 to 0.88) than when pooled, as mean bias varied by land cover type. Wetlands had slightly larger bias (−3.2 K), RMSE (3.6 K), and lower correlation than the forested areas.

When the high-resolution LST was compared to independent satellite estimates of LST, a single Landsat scene generally revealed similar correspondence in primary spatial pattern, but overall correlation of the two products was much lower (r^2=0.27, Fig. 6). The correlation was strongly influenced by underestimation of higher LST range of the observation by our fusion product, over urban areas and a few forest clearings, implying an alternate weighting scheme may allow for better correspondence in those locations which are less prevalent in the area and thus under-represented in the calibration. As well, outside of those areas, variance of LST on this particular mid-day mid-summer scene is relatively small, within the RMSE shown for the high-resolution LST in the tower and aircraft comparison.

3.4 Additional downscaling

Ultra-high-resolution downscaling to 10 m required additional inputs at fine resolution. In this case, visible to near infrared hyperspectral observations provided useful information to explain sub-grid anomalies in the high-resolution 50 m LST. NDSI plots demonstrate a number of bands where visible and infrared band differences highly correlate with anomalies in subgrid LST as observed by the drone (Fig. 7). Most of the normalized differences with high correlation were on bands that were near each other, reflecting the role of specific spectral reflectance features of vegetation and soils that relate to LST variation. Here, we selected the top three consistent correlated NDSI band differences across the three flights. The three band pairs were: 1982.7 nm and 1470.5 nm in the shortwave infrared (NDSI_SWIR, r = 0.380), 709.1 nm and 760.2 nm in the red-edge spectral region (NDSI_EDGE, r=0.448), and 651.6 nm and 504.7 nm at the red-green portions of the visible spectrum (NDSI_VIS, r=0.442). In all three combinations, the second listed wavelength was subtracted from the first. The latter two are close to commonly used vegetation indices of NDVI (typically 630-690 nm and 760-900 nm) and the photochemical reflectance index (PRI, 531 nm and 571 nm), and correlations in those bands are not too far off from the selected bands (boxes in Fig. 7), consistent to other studies linking LST and vegetation indices (e.g., Raynolds *et al*., 2008; Karnieli *et al*., 2010). With these three bands, a linear model was built to explain the subgrid LST anomalies and applied to the downscaled LST_50m (Fig. 8), expressed as:

$$\text{LST\_10m} = 2.147 \times \text{NSDI\_SWIR} + 3.826 \times \text{NDSI\_EDGE} + 5.143 \times \text{NDSI\_VIS} + 4.566 + \text{LST\_50m} \quad \text{(Equation 2)}$$

The resulting model produced an ultra-high resolution LST map that was reasonably correlated to the drone imagery (r^2=0.34) and had significantly reduced bias compared to the 50 m LST from 2.35 K to near zero, and lower bias-removed RMSE from 3.0 K to 1.7 K. Most NDSI_SWIR values were positive (mean 0.12 +/- 0.07), while NDSI_EDGE (-0.59 +/- 0.10) and NDSI_VIS (-0.48 +/- 0.09) were negative. Since all three coefficients were positive, the effect of positive SWIR was to increase LST, while for the mostly negative red-edge or visible reflectance was to decrease LST. The effect of these is to bring out key LST features, especially on the "hot-spot" side, such as a road and a larger open area, both of which were observed to have high LST but not well-detected in the original downscaled image. The higher NDSI_SWIR of these two features allowed this model to better capture its higher LST. The results paint a multi-step pathway toward downscaling LST to meter scale resolution.

4. Discussion

Land surface temperature exhibits high spatial and temporal variability. Depending on the application, capturing this variability can be essential for diagnosing land-atmosphere interactions, soil processes, and ecosystem thermal tolerances. Here, we demonstrated one approach to capture these scales of variations with multi-sensor fusion and find high skill in these when compared against independent LST observations. Both direct observations of LST and indirect observations of covariates provided information needed to downscale to hourly, 10 m resolution LST.

4.1 Challenges in LST fusion

Our LST fusion approach performed well on evaluation, but several lingering uncertainties remain which require further investigation. The first involves the gap-filling of cloud cover. Previous satellite fusion investigations generally focused on clear-sky LST. The primary assumption made in our methodology is that the relatively strong linear relationship of pixel-level, hour-segregated NLDAS modeled LST, which does incorporate the effect of clouds into its LST estimates (at least as reflected in the input model forcing), to the cloud-screened GOES is translatable to gap-filling. This approach assumes that LST during cloud cover is similar to LST during clear-sky conditions, given the same temperature for that time of day. Generally, the effect of clouds is to make LST cooler in daytime and warmer in nighttime compared to clear-sky. An analysis of cloud cover (estimated as ratio of observed shortwave radiation to potential maximum shortwave) versus difference in fusion to tower observed LST did not show any clear trend, suggesting this assumption is broadly reasonable.

Downscaling with ECOSTRESS and a linear model also brings additional uncertainty. The coverage of ECOSTRESS varies by time of day and cloud cover, which means that each pixel had differing numbers of valid ECOSTRESS LST observations across the study period. Here we assume no change in seasonality of the relationship or temporal differences. Rather, we assume that what ECOSTRESS is mainly providing is differences in mean LST within the subgrid of a single GOES pixel (intercept) and changes in the diel amplitude (slope). However, this assumes that other biases are negligible, no changes occurred in land surface from disturbance, and seasonal variation in those two factors are zero. Subsetting by sub-season would be helpful here, but given the repeat interval and number of cloud-free images, statistical power would degrade noticeably. With a longer time period dataset, additional subsetting may be warranted to evaluate such an approach. While some aspects may have been better captured using a non-linear model, deviation from linear slopes across our ECOSTRESS and GOES pairs was rarely seen and initial tests with quadratic forms did not find improved fits. Data mining approaches, including data sharpening approaches, may improve performance (Gao *et al*., 2012).

Some of these performance issues show up when looking at the goodness of fit against towers and aircraft, and in the diel cycle plots. While the downscaling helps differentiate variation in LST by land cover type, it appears the methodology has challenges with a few land cover types. One is lakes, and especially lake-land edges, where pixel registration and gradients are missed leading to increased “noise” or blur in images around lakes. However, visual inspection of geolocation errors did not find anything significantly skewed. The second is picking up cold LST values in autumn. The drone comparisons also suggest that the 70 m resolution of ECOSTRESS may still be challenging for picking up even finer-scale urban, road, or other hot spots on the landscape.

View angle differences among the sensors may also contribute to differing error structures and biases that were not corrected in the provided Level 2 products used here (Anderson *et al*., 2021; Ermida *et al*., 2014; Gerace *et al*., 2020; Guillevic *et al*., 2013;). Geostationary satellites in particular have strong angular effects as the sensor scans away from the central location, while ECOSTRESS has a +/- 25 degree acceptance swath, narrower than other polar orbiters. Surface skin temperature is also derived from different sets of wavelengths across the sensors and biases

from these may pose a challenge in addition to algorithmic differences in retrievals (Bosilovich *et al*., 2007). It is one reason we used mean bias removal in our regressions.

4.2 Mechanisms of LST relationships to visible to VSWIR spectra

Though limited to a small number of images, our attempt to further downscale with visible to shortwave infrared hyperspectral imagery demonstrated improved ability to resolve fine-scale features such as roads and smaller wetlands observed in the drone imagery. The three band indices that contributed most to the NDSI regression represent key vegetation and soil features that link to LST variation. The strongest was in the shortwave IR, a region known to detect differences in soil thermal and moisture status. The other two in the visible and red-edge reflect signals of vegetation presence and photosynthetic activity, respectively. Actively photosynthesizing vegetation will have lower LST due to the cooling effect of concomitant transpiration and given our formulation of NDSI, those areas had higher negative values in NDSI_EDGE and NDSI_VIS, which when combined with positive coefficients, led to lower LST over vegetated areas. The SWIR bands helped distinguish areas of exposed ground, and NDSI_SWIR was found to be most strongly positive over roads and open area. The broad areas of high correlation also partly overlap with commonly used band ratios including NDVI and PRI, suggesting that broadband visible-IR remote sensing has strong potential for downscaling LST.

4.3 Comparison to other approaches

While several papers have assessed fusion approaches for gridded LST, literature on joint temporal and spatial LST downscaling is relatively limited, with primary applications over urban areas (e.g., Sismanidis et al., 2016a,b, 2018). Our results show that sub-daily temporal and sub-km spatial downscaling is possible while maintaining a similar level of uncertainty as previously published daily or less-frequent LST products (Freitas *et al*., 2010, Goettsche *et al*., 2013). Further, even without the additional spatialization from ECOSTRESS or HySpex, there is significant value in greater use of geostationary satellite LST. Several of these satellites can now provide up to one-minute time resolution for target-mode operations, and fusion of these through a data assimilation approach would help develop global high-temporal resolution LST (Freitas *et al*., 2013; Xiao et al., in press). Further work on using the higher frequency observations to reduce cloud coverage and increase estimate of temperature variability could prove useful for developing more sub-daily LST related products, including surface energy fluxes.

4.4 Applications of high space and time resolution LST

There is a downside with temporal and spatial downscaling of LST, which is the increase in uncertainty as more products are fused and local calibrations fail to extrapolate well. The higher uncertainty does lead to the question of whether such an approach adds value. Beyond the aforementioned importance of fine space and time variation in LST for biological and geophysical processes, a number of studies suggests that higher resolution LST, even with greater uncertainty, aids in interpreting observations and testing hypotheses.

For example, the Environmental Response Function approach is a method to map surface-atmosphere fluxes of carbon, energy, and momentum across space and time from fusion of eddy

546 covariance flux towers, flux footprint models, and input covariates (Metzger *et al*., 2013; Xu *et*
547 *al*., 2017). For surface energy fluxes such as sensible heat flux, LST is a key driver. Eddy fluxes
548 of sensible heat during periods of high variability in wind direction reveal the presence of hot
549 spots and hot moments of heat flux across space. The ERF methodology can identify those only
550 if the input covariates are of sufficient spatial (decameter) and temporal (hourly or better)
551 resolution to resolve those. While these flux hot spots can be tied to landscape features, they also
552 can be transient features of atmospheric circulation. Previous ERF studies relied on linear
553 regridding of coarser resolution LST products, decreasing the accuracy of hot spot localization
554 (e.g., Xu *et al*., 2017). Thus, even at acceptance of higher random uncertainty, a high space and
555 time LST product is essential in this application. The variation in LST or difference of LST to air
556 temperature is fit to an empirical model. Thus, it is the variation in LST that is guiding the
557 methods, and accuracy is less important than spatial precision. In other cases, the magnitude of
558 LST may be the driving factor, as is the case in models of evapotranspiration (Anderson *et al*.,
559 2021; Guillevic *et al*., 2019) or atmospheric boundary-layer growth (Desai *et al*., 2006), in which
560 case, the additional spatial information may be of less use, but the higher temporal information
561 captures land-surface heat capacity and moisture holding impacts that influence the diel cycle of
562 LST.
563
564 There are other cases where neither the variation nor magnitude matters, but rather the spatial
565 structure. Consider Fig. 9, where we depict the radially integrated spatial power spectrum of LST
566 from GOES-NLDAS, ECOSTRESS, and the fused product. A number of fine scale modes of
567 variation are present in the higher resolution products not found in GOES, which overestimates
568 the autocorrelation. Similarly, when looking over time (Fig. 10), the enhanced spatial resolution
569 improves upon GOES ability to detect increasing spatial variation of LST in autumn and during
570 the mid-day in summer. These patterns have been tied to generating heterogeneity in heat fluxes
571 that promote mesoscale atmospheric circulations (Butterworth *et al*., 2021).

572 5. Conclusions

573 We demonstrated that a fusion of modeled land surface temperature with geostationary, irregular,
574 and polar orbit observations and hyperspectral imagery provides a simple pathway for high space
575 and time resolution LST for any region where those observations are available. LST estimates
576 well captured many dynamics of spatial and temporal variation across a heterogeneous landscape
577 of lakes, forests, wetlands, and urban areas in northern Wisconsin. Additional efforts should be
578 placed on approaches to gap-filling for clouds, improvement of LST retrievals over water bodies
579 and landscape transition edges, and multi-instrument evaluation. Our results suggest that
580 continued effort to combine temporal and spatial estimates of LST can provide a fruitful path
581 forward to better understand earth system processes, land surface data assimilation for modeling,
582 and microclimate delineation.

583 Acknowledgments

584 We thank the many data providers who helped extract observations including the National
585 Center for Atmospheric Research (NCAR) Integrated Surface Flux Facility team, the University
586 of Wyoming King Air team, and NOAA ATDD UAS team, including S. Oncley of NCAR and

D. Plummer from U Wyoming. The CHEESEHEAD19 field study would not have been possible without the tremendous amount of work from dozens of colleagues. CHEESEHEAD19 was supported by NSF #1822420. The National Ecological Observatory Network is a program sponsored by the National Science Foundation and operated under cooperative agreement by Battelle. This material is based in part upon work supported by the National Science Foundation through the NEON Program. JBF and GH contributed to this research at the Jet Propulsion Laboratory, California Institute of Technology, under a contract with the National Aeronautics and Space Administration. California Institute of Technology. Government sponsorship acknowledged. JBF and GH were supported by NASA ECOSTRESS and PCS was supported by NSF #2034997.

Data

CHEESEHEAD19 observations from flux towers and aircraft, NOAA UAS drone LST, UW HySpex hyperspectral imagery, and the derived land surface temperature grids are available at the National Center for Atmospheric Research (NCAR) Earth Observing Lab (EOL) data repository at: https://www.eol.ucar.edu/field_projects/cheesehead. A direct link to the derived 50 m LST is https://doi.org/10.26023/5J4W-8XPH-250N. ECOSTRESS observations can be obtained from: https://ecostress.jpl.nasa.gov/data . NLDAS model outputs are available at: https://disc.sci.gsfc.nasa.gov/datasets?keywords=NLDAS . GOES ABI LST data are at: https://www.ncei.noaa.gov/access/metadata/landing-page/bin/iso?id=gov.noaa.ncdc:C01521 . The LST fusion algorithm is available at: https://github.com/DesaiLab/LSTfusion

Works Cited

Adler-Golden, S. M., Matthew, M. W., Bernstein, L. S., Levine, R. Y., Berk, A., *et al*., 1999. Atmospheric correction for shortwave spectral imagery based on MODTRAN4, in *Imaging Spectrometry V*, 3753, 61-69. International Society for Optics and Photonics.

Anderson, M., Yang, Y., Xue, J., Knipper, K.R., Yang, Y., Gao, F., Hain, C.R., Kustas, K.P., Cawse-Nicholson, K., Hulley, G., Fisher, J.B., Alfieri, J.G., Meyers, T.P., Prueger, J., Baldocchi, D.D., Rey-Sanchze, C., 2021. Interoperability of ECOSTRESS and Landsat for mapping evapotranspiration time series at sub-field scales, *Remote Sensing of Environment*, 252, 112189, doi:10.1016/j.rse.2020.112189.

Bosilovich, M.G., Radakovich, J.D., da Silva, A., Todling, R., and Verter, F., 2007. Skin temperature analysis and bias correction in a coupled land-atmosphere data assimilation system, *J. Meteor. Soc. Jap.*, 85A, 205-228.

Bütikofer, L., Anderson, K., Bebber, D.P., Bennie, J.J., Early, R.I., Maclean, I.M.D., 2020. The problem of scale in predicting biological responses to climate, *Glob. Change Biol.*, 26, 6657– 6666, doi:10.1111/gcb.15358.

Butterworth, B.J., Desai, A.R., Metzger, S., Townsend, P.A., Schwartz, M.D., Petty, G.W., Mauder, M., Vogelmann, H., Andresen, C.G., Augustine, T.J., Bertram, T.H., Brown, W.O.J., Buban, M., Cleary, P., Durden, D.J., Florian, C.R., Ruiz, E.G., Iglinski, T.J.,

Kruger, E.L., Lantz, K., Lee, T.R., Meyers, T.P., Mineau, J.K., Olson, E.R., Oncley, S.P., Paleri, S., Pertzborn, R.A., Pettersen, C., Plummer , D.M., Riihimaki, L., Sedlar, J., Smith, E.N., Speidel, J., Stoy, P.C., Sühring, M., Thom, J.E., Turner, D.D., Vermeuel, M.P., Wagner, T.J., Wang, Z., Wanner, L., White, L.D., Wilczak, J.M.M., Wright, D.B., and Zheng, T., 2021. Connecting Land-Atmosphere Interactions to Surface Heterogeneity in CHEESEHEAD19, *Bulletin of the American Meteorological Society*, 102, E421-E445, doi:10.1175/BAMS-D-19-0346.1.

Chen, F., Mitchell, K., Schaake, J., Xue, Y., Pan, H.-L., Koren, V., Duan, Q. Y., Ek, M., and Betts, A., 1996. Modeling of land surface evaporation by four schemes and comparison with FIFE observations, *J. Geophys. Res*., 101(D3), 7251– 7268, doi:10.1029/95JD02165.

Dirmeyer, P.A., Cash, B.A., Kinter III, J.L., Jung, T., Marx, L., Stan, C., Towers, P., Wedi, N., Adams, J.M., Altshuler, E.L., Huang, B. , Jin, E.K., and Manganello, J., 2012, Evidence for enhanced land-atmosphere feedback in a warming climate, *J. Hydrometeor.,* 13, 981-995, doi: 10.1175/JHMD-11-0104.1.

Dubois, S., Desai, A.R., Singh, A., Serbin, S., Goulden, M., Baldocchi, D., Ma, S., Oechel, W., Wharton, S., Kruger, E., and Townsend, P., 2018. Using imaging spectroscopy to detect variation in terrestrial ecosystem productivity across a water-stressed landscape, *Ecological Applications*, 28, 1313-1324, doi:10.1002/eap.1733.

Dumas, E.J., Lee, T.R, Buban, M., and Baker, B., 2016. Small Unmanned Aircraft System (sUAS) measurements during the 2016 Verifications of the Origins of Rotation in Tornadoes Experiment Southeast (VORTEX-SE), *NOAA Technical Memorandum,* OAR ARL-273.

Dumas, E.J., Lee, T.R., Buban, M., and Baker, B., 2017. Small Unmanned Aircraft System (sUAS) measurements during the 2017 Verifications of the Origins of Rotation in Tornadoes Experiment Southeast (VORTEX-SE), *NOAA Technical Memorandum,* OAR ARL-274.

English, S.J. ,2008. The importance of accurate skin temperature in assimilation radiances from satellite sounding instruments, *IEEE Trans. Geosc. Sens*., 46, 403-408, doi:10.1109/TGRS.2007.902413.

Ermida, S.L., I.F. Trigo, C.C. DaCamara, F.M. Göttsche, F.S. Olesen and G. Hulley (2014), Validation of remotely sensed surface temperature over an oakwood landscape - The problem of viewing and illumination geometries. Remote Sens. Env., 148, 16-27, doi: dx.doi.org/10.1016/j.rse.2014.03.016.

Fisher, J.B., Lee, B., Purdy, A.J., Halverson, G.H., Dohlen, M.B., Cawse-Nicholson, K., Wang, A., Anderson, R.G., Aragon, B., Arain, M.A., Baldocchi, D.D., Baker, J.M., Barral, H., Bernacchi, C.J., Bernhofer, C., Biraud, S.C., Bohrer, G., Brunsell, N., Cappelaere, B., Castro-Contreras, S., Chun, J., Conrad, B.J., Cremonese, E., Demarty, J., Desai, A.R., De Ligne, A., Foltýnová, L., Goulden, M.L., Griffis, T.J., Grünwald, T., Johnson, M.S., Kang, M., Kelbe, D., Kowalska, N., Lim, J.H., Maïnassara, I., McCabe, M.F., Missik, J.E.C., Mohanty, B.P., Moore, C.E., Morillas, L., Morrison, R., Munger, J.W., Posse, G.,

Richardson, A.D., Russell, E.S., Ryu, Y., Sanchez-Azofeifa, A., Schmidt, M., Schwartz, E., Sharp, I., Sˇigut, L., Tang, Y., Hulley, G., Anderson, M., Hain, C., French, A., Wood, E., Hook, S., 2020. ECOSTRESS: NASA's next generation Mission to measure evapotranspiration from the international Space Station, *Water Resour. Res.*, 56, e2019WR026058, doi:10.1029/2019WR026058.

Freitas, S.C., Trigo, I.F., Bioucas-Dias, J.M., and Goettsche, F.-M. ,2010. Quantifying the Uncertainty of Land Surface Temperature Retrievals From SEVIRI/Meteosat, *IEEE Trans. Geosci. Remote Sens.*, doi:10.1109/TGRS.2009.2027697.

Freitas, S.C., Trigo, I.F., Macedo, J., Barroso, C., Silva, R., and Perdigão, R., 2013. Land surface temperature from multiple geostationary satellites, *International Journal of Remote Sensing*, 34, 3051-3068, doi:10.1080/01431161.2012.716925.

Gao, F., Hilker, T., Zhu, X., Anderson, M., Masek, J., Wang, P., & Yang, Y., 2015. Fusing Landsat and MODIS Data for Vegetation Monitoring, *IEEE Geoscience and Remote Sensing Magazine*, 3, 47-60, doi:10.1109/mgrs.2015.2434351.

Gao, F., Kustas, W.P., Anderson, M.C., 2012. A data mining approach for sharpening thermal satellite imagery over land, *Remote Sens*., 4, 3287–3319.

Gao, F., Masek, J., Schwaller, M., and Hall, F., 2006. On the blending of the Landsat and MODIS surface reflectance: predicting daily Landsat surface reflectance, IEEE Transactions on Geoscience and Remote Sensing, 44, 2207-2218, doi:10.1109/tgrs.2006.872081.

Gerace, A., Kleynhans, T., Eon, R., Montanaro, M., 2020. Towards an Operational, Split Window-Derived Surface Temperature Product for the Thermal Infrared Sensors Onboard Landsat 8 and 9, *Remote Sensing*, 12, 224, doi:10.3390/rs12020224.

Gillespie, A., Rokugawa, S., Matsunaga, T., Steven Cothern, J., Hook, S., Kahle, A.B., 1998. A temperature and emissivity separation algorithm for advanced spaceborne thermal emission and reflection radiometer (ASTER) images, *IEEE Trans. Geosci. Remote Sens*. 36, 1113–1126.

Gillespie, A., Rokugawa, S., Matsunaga, T., Cothern, J.S., Hook, S., and Kahle, A.B., 1998. A temperature and emissivity separation algorithm for Advanced Spaceborne Thermal Emission and Reflection Radiometer (ASTER) images, *IEEE Transactions on Geoscience and Remote Sensing*, 36, 1113-1126, doi: 10.1109/36.700995.

Goettsche, F.M., Olesen, F.S., and Bork-Unkelbach, A., 2013. Validation of land surface temperature derived from MSG/SEVIRI with in situ measurements at Gobabeb, Namibia, *Int. J. Remote Sens*, 34, 3069-3083, doi: 10.1080/01431161.2012.716539.

Guillevic, P.C., *et al* ., 2013. Directional Viewing Effects on Satellite Land Surface Temperature Products Over Sparse Vegetation Canopies—A Multisensor Analysis, *IEEE Geoscience and Remote Sensing Letters*, 10, 1464-1468, doi: 10.1109/LGRS.2013.2260319.

Guillevic, P.C., Olioso, A., Hook, S.J., Fisher, J.B., Lagouarde, J.P., Vermote, E.F., 2019. Impact of the revisit of thermal infrared remote sensing observations on evapotranspiration uncertainty-a sensitivity study using AmeriFlux data, *Remote Sens.* 11, 573.

Hu, Y., Tani, R.,Jiang, X., Li, vZ. -L., Jiang, Y., and Liu, M., 2020. Spatial Downscaling of Land Surface Temperature based On Surface Energy Balance, 2020 *IEEE International Geoscience and Remote Sensing Symposium (IGARSS)*, Waikoloa, HI, USA, 4926-4929, doi: 10.1109/IGARSS39084.2020.9323945.

Hulley, G.C. and Ghent, D., 2019. *Taking the Temperature of the Earth: Steps towards integrated understanding of variability and change*. Amsterdam, Netherlands: Elsevier, 2019, p. 256.

Hulley, G.C., and Hook, S.J., 2011. Generating Consistent Land Surface Temperature and Emissivity Products Between ASTER and MODIS Data for Earth Science Research, *IEEE Transactions on Geoscience and Remote Sensing*, 49, 1304-1315

Hulley, G., Hook, S., Fisher, J., and Lee, C., 2017. ECOSTRESS, A NASA Earth-Ventures Instrument for studying links between the water cycle and plant health over the diurnal cycle, 2017 *IEEE International Geoscience and Remote Sensing Symposium (IGARSS)*, Fort Worth, TX, 5494-5496, doi:10.1109/IGARSS.2017.8128248.

Hulley, G.C., Goettsche, F., Rivera, G., Hook, S., Freepartner, R., Radocinski, R., Martin, M., Cawse-Nicholson, K., Johnson, W., 2021. Validation and quality assessment of the ECOSTRESS level-2 land surface temperature and emissivity product, *IEEE TGRS*, in press.

Kabsch, E., Olesen, F.S. and Prata, A.J., 2008. Initial results of the land surface temperature (LST) validation with the Évora, Portugal ground-truth station measurements, *Int. J. Remote Sensing*, 29, 5329- 5345.

Karnieli, A., Agam, N., Pinker, R. T., Anderson, M., Imhoff, M. L., Gutman, G. G., Panov, N., & Goldberg, A., 2010. Use of NDVI and Land Surface Temperature for Drought Assessment: Merits and Limitations, *Journal of Climate*, *23*(3), 618-633.

Khan, A.M., Stoy, P.C., Douglas, J.T., Anderson, M., Diak, G., Otkin, J.A., Hain, C., Rehbein, E. M., and McCorkel, J., 2021. Reviews and syntheses: Ongoing and emerging opportunities to improve environmental science using observations from the Advanced Baseline Imager on the Geostationary Operational Environmental Satellites, *Biogeosciences Discuss.* doi:10.5194/bg-2020-454, in review.

Koster, R.D., and Suarez, M.J., 1992. Modeling the land surface boundary in climate models as a composite of independent vegetation stands, *J. Geophys. Res.-Atmosphere*, 97, 2697-2715, doi:10.1029/91JD01696.

Kröniger, K., Katul, G.G., De Roo, F., Brugger, P., and Mauder, M., 2019. Aerodynamic Resistance Parameterization for Heterogeneous Surfaces Using a Covariance Function Approach in Spectral Space, *Journal of the Atmospheric Sciences*, 76, 3191-3209.

742 Landsman, W.B, 1993. Astronomical Data Analysis Software and Systems II, *A.S.P. Conference*
743 *Series*, 52, ed. R.J. Hanisch, R.J.V. Brissenden, and J. Barnes, p. 246.

744 Lee, T.R., Buban, M., Dumas, E., and Baker, C.B., 2017. A new technique to estimate sensible
745 heat fluxes around micrometeorological towers using small unmanned aircraft systems,
746 *Journal of Atmospheric and Oceanic Technology*, 34, 2103-2112, doi:10.1175/JTECH-D-
747 17-0065.1.

748 Lee, T R., Buban, M., Dumas, E., and Baker, C.B., 2019. On the use of rotary-wing aircraft to
749 sample near-surface thermodynamic fields: results from recent field campaigns, *Sensors*,
750 19, 10, doi:10.3390/s19010010.

751 Li, Z., Tang, B.-H., Wu, H., Ren, H., Yan, G., Wan, Z., Trigo, I.F., Sobrino, J.A., 2013. Satellite-
752 derived land surface temperature: Current status and perspectives, *Remote Sensing of*
753 *Environment*, 131,14-37, doi:10.1016/j.rse.2012.12.008.

754 Liang, X., Lettenmaier, D.P., Wood, E F., and Burges, S.J., 1994. A simple hydrologically based
755 model of land surface water and energy fluxes for general circulation models, *J. Geophys.*
756 *Res.-Atmospheres*, 99, 14415-14428, doi:10.1029/94JD00483.

757 Liu, Y., T. Hiyama and Yamaguchi, Y., 2006. Scaling of land surface temperature using satellite
758 data: A case examination on ASTER and MODIS products over a heterogeneous terrain
759 area, *Remote Sens. Env.*, 105, 115-128, doi:10.1016/j.rse.2006.06.012.

760 Liu, N., Chlus, A., Townsend, P.A., 2019. HyToolsPro: An open source package for pre-
761 processing airborne hyperspectral images. In: 2019 Fall Meeting AGU. San Francisco,
762 CA, pp. GC51E–1120. https://github.com/EnSpec/hypro

763 Malakar, N. K., Hulley, G.C., Laraby, K., Cook, M., Hook, S., and Schott, J., 2018. An
764 Operational Land Surface Temperature Product for Landsat Thermal Data: Methodology
765 and Validation, *IEEE TGRS*, 56 (10), pp. 5715-5735, doi:10.1109/TGRS.2018.2824828.

766 Matricardi, M., 2008. The generation of RTTOV regression coefficients for IASI and AIRS
767 using a new profile training set and a new line-by-line database. In: ECMWF Research
768 Dept. Tech. Memo.

769 Mauder, M., Desjardins, R.L., and MacPherson, I. 2007. Scale analysis of airborne flux
770 measurements over heterogeneous terrain in a boreal ecosystem, *J. Geophys. Res.*, 112,
771 D13112, doi:10.1029/2006JD008133.

772 Metzger, S., 2018. Surface-atmosphere exchange in a box: Making the control volume a suitable
773 representation for in-situ observations, *Agric. For. Meteorol.*, 255, 68-80,
774 doi:10.1016/j.agrformet.2017.08.037.

775 Metzger, S., Junkermann, W., Mauder, M., Butterbach-Bahl, K., Trancón y Widemann, B.,
776 Neidl, F., Schäfer, K., Wieneke, S., Zheng, X. H., Schmid, H. P., and Foken, T., 2013.
777 Spatially explicit regionalization of airborne flux measurements using environmental
778 response functions, *Biogeosciences*, 10, 2193–2217, https://doi.org/10.5194/bg-10-2193-
779 2013.

780 Pincebourde, S., and Salle, A., 2020. On the importance of getting fine-scale temperature records
781 near any surface, *Glob Change Biol*., 26, 6025– 6027, doi:10.1111/gcb.15210

782 Raynolds, M. K., Comiso, J. C., Walker, D. A., and Verbyla, D., 2008. Relationship between
783 satellite-derived land surface temperatures, arctic vegetation types, and NDVI, Remote
784 Sensing of Environment, 112, 1884-1894, doi: 10.1016/j.rse.2007.09.008.

785 Saunders, R., Matricardi, M., and Brunel, P. ,1999. An improved fast radiative transfer model for
786 assimilation of satellite radiance observations, *Quarterly Journal of the Royal*
787 *Meteorological Society*, 125, 1407-1425.

788 Scarino B., Minnis, P., Palikonda, R., Reichle, R.H., Morstad, D., Yost, C., Shan, B., and Liu,
789 Q., 2013. Retrieving Clear-Sky Surface Skin Temperature for Numerical Weather
790 Prediction Applications from Geostationary Satellite Data, *Remote Sens.*, 5, 342-366,
791 doi:10.3390/rs5010342.

792 Schläpfer, D., and Richter, R., 2002. Geo-atmospheric processing of airborne imaging
793 spectrometry data. Part 1: Parametric orthorectification, *International Journal of Remote*
794 *Sensing*, 23, 2609-2630, doi:10.1080/01431160110115825.

795 Schmit, T.J., Griffith, P., Gunshor, M.M., Daniels, J.M., Goodman, S.J., and Lebair, W. J., 2017.
796 A Closer Look at the ABI on the GOES-R Series, *Bulletin of the American*
797 *Meteorological Society*, 98, 681-698, doi:10.1175/BAMS-D-15-00230.1.

798 Silvestri, M., Romaniello, V., Hook, S., Musacchio, M., Teggi, S., Buongiorno, M.F., 2020. First
799 Comparisons of Surface Temperature Estimations between ECOSTRESS, ASTER and
800 Landsat 8 over Italian Volcanic and Geothermal Areas, *Remote Sens.*, 12, 184,
801 doi:10.3390/rs12010184

802 Sismanidis, P., Bechtel, B., Keramitsoglou, I., Kiranoudis, C.T., 2018. Mapping the
803 spatiotemporal dynamics of Europe's land surface temperatures*, IEEE Geoscience and*
804 *Remote Sensing Letters*, 15, 202-206, doi:10.1109/LGRS.2017.2779829.

805 Sismanidis, P., Keramitsoglou, I., Bechtel, B., Kiranoudis, C., 2016a. Improving the downscaling
806 of diurnal land surface temperatures using the annual cycle parameters as disaggregation
807 kernels, *Remote Sensing* 9, 23, doi:10.3390/rs9010023.

808 Sismanidis, P., Keramitsoglou, I., Kiranoudis, C., Bechtel, B., 2016b. Assessing the capability of
809 a downscaled urban land surface temperature time series to reproduce the spatiotemporal
810 features of the original data, *Remote Sensing* 8, 274. doi:10.3390/rs8040274.

811 Taylor, C.M., de Jeu, R.A.M., Guichard, F., Harris, P.P., and Dorigo, W.A., 2012. Afternoon
812 rain more likely over drier soils. *Nature*, 489, 423-426, doi:10.1038/nature11377.

813 Tomlinson, C.J., Chapman, L., Thornes, J.E. and Baker, C., 2011. Remote sensing land surface
814 temperature for meteorology and climatology: a review, *Met. Apps*, 18, 296-306,
815 doi:10.1002/met.287

816 Trigo, I.F., Monteiro, I.T., Olesen, F., and Kabsch, E., 2008. An assessment of remotely sensed
817 land surface temperature, *J. Geophys. Res.*, 113, D17108, doi:10.1029/2008JD010035.

818 Wang, A., Barlage, M., Zeng, X., and Draper, C.S., 2014. Comparison of land skin temperature
819 from a land model, remote sensing and in situ measurement, *J. Geophys. Res.*, 119, 3093-
820 3106, doi:10.1002/2013JD021026.

821 Xia, Y., *et al*., 2012. Continental-scale water and energy flux analysis and validation for the
822 North American Land Data Assimilation System project phase 2 (NLDAS-2): 1.
823 Intercomparison and application of model products, *J. Geophys. Res.*, 117, D03109,
824 doi:10.1029/2011JD016048.

825 Xiao, J., Fisher, J.B., Hashimoto, H., Ichii, K., Parazoo, N.C., in press. Emerging satellite
826 observations for diurnal cycling of ecosystem processes. *Nature Plants*.

827 Xu, K., Metzger, S., Desai, A.R., 2017. Upscaling tower-observed turbulent exchange at fine
828 spatio- temporal resolution using environmental response functions, *Agricultural and*
829 *Forest Meteorology*, 232, 10-22, doi:10.1016/j.agrformet.2016.07.019.

830 Xu, K., Metzger, S., and Desai, A. R., 2018. Surface-atmosphere exchange in a box:
831 Space-time resolved storage and net vertical fluxes from tower-based eddy covariance,
832 *Agric. For. Meteorol.*, 255, 81-91, doi:10.1016/j.agrformet.2017.10.011.

833 Xu, K., Sühring, M., Metzger, S., Durden,D., Desai, A.R., 2020. Can data mining help eddy-
834 covariance see the landscape? A large-eddy simulation study, *Boundary-Layer*
835 *Meteorology,* 176, 85-103, doi:10.1007/s10546-020-00513-0.

836 Xu, T., Bateni, S.M., Neale, C.M.U., Auligne, T., and Liu, S., 2018. Estimation of turbulent heat
837 fluxes by assimilation of land surface temperature observations from GOES satellites into
838 an ensemble Kalman smoother framework, *Journal of Geophysical Research:*
839 *Atmospheres*, 123, 2409– 2423, doi:10.1002/2017JD027732.

840 Yi, K., Smith, J., Jablonsk, A., Tatham, E., Scanlon, T., Lerdau, M., Novick, K., Yang, X., 2020.
841 High heterogeneity in canopy temperature among co-occurring tree species in a
842 temperate forest, *Journal of Geophysical Research-Biogeosciences*, 125,
843 e2020JG005892, doi:10.1029/2020JG005892.

844 Yu, Y., *et al*., 2009. Developing Algorithm for Operational GOES-R Land Surface Temperature
845 Product, *IEEE Transactions on Geoscience and Remote Sensing*, 47, 936-951, doi:
846 10.1109/TGRS.2008.2006180.

847 Yu, Y., *et al*., 2012. Validation of GOES-R Satellite Land Surface Temperature Algorithm Using
848 SURFRAD Ground Measurements and Statistical Estimates of Error Properties, *IEEE*
849 *Transactions on Geoscience and Remote Sensing*, 50, 704-713,
850 doi:10.1109/TGRS.2011.2162338.

851 Yue *et al*., 2020. Sharpening ECOSTRESS and VIIRS land surface temperature using
852 harmonized Landsat-Sentinel surface reflectances, *Remote Sensing of Environment*, 251,
853 112055, doi:10.1016/j.rse.2020.112055.

854 Zheng, W., Wei, H., Wang, Z., Zeng, X., Meng, J., Ek, M., Mitchell, K., and Derber, J., 2012.
855 Improvement of daytime land surface skin temperature over arid regions in the NCEP

856 GFS model and its impact on satellite data assimilation, *J. Geophys. Res*, 117, D06117,
857 doi:10.1029/2011JD015901.

Tables

Table 1. Input data sources used in gap-filling and downscaling land surface temperature

Product	Description	Spatial Resolution	Temporal Repeat Frequency	URL
NLDAS-2	Data-assimilation model reanalysis LST	⅛ degree	hourly	https://ldas.gsfc.nasa.gov/nldas/
GOES-R	Geostationary satellite LST over Western Hemisphere	~2 km	15 minutes	https://www.goes-r.gov/products/baseline-LST.html
ECOSTRESS	Thermal imager on International Space Station	70 m × 70 m	1-5 day; diurnal sampling	https://ecostress.jpl.nasa.gov/
UW HySpex	Visible to Shortwave IR airborne hyperspectral imager 400-2500 nm	Varies, ~1 m	~Monthly	https://data.eol.ucar.edu/dataset/592.027

862 **Table 2**. Evaluation data sources
863

Product	**Description**	**Spatial Resolution**	**Temporal Repeat Frequency**	**URL**
University of Wyoming King Air (UWKA)	Upwelling infrared surface temperature	~10 m	Twice-daily over three 4-day periods	http://flights.uwyo.edu/projects/cheesehead19/
NCAR Integrated Surface Flux Station (ISFS)	Upwelling longwave radiation from 19 eddy covariance towers	~50 m	5-minute average	https://data.eol.ucar.edu/dataset/592.025
Landsat Two-source LST	Satellite land surface temperature	30 m	~16 day	https://doi.org/10.3390/rs12020224
NOAA UAS	Drone based land surface temperature	Varies, ~1 m	Hourly in daytime over two 4-day periods	https://data.eol.ucar.edu/dataset/592.010

864

Figures

Figure 1. Stommel diagram schematic of space and time scale of input data products (black text), evaluation LST (cyan), high-resolution (50 m) and ultra-high-resolution (10 m) downscaled LST (dark blue), and processes to create those (red arrows and text) over the CHEESEHEAD19 domain (map, upper right, and red box). Example input LST imagery is shown from 7 Aug 2019 0Z.

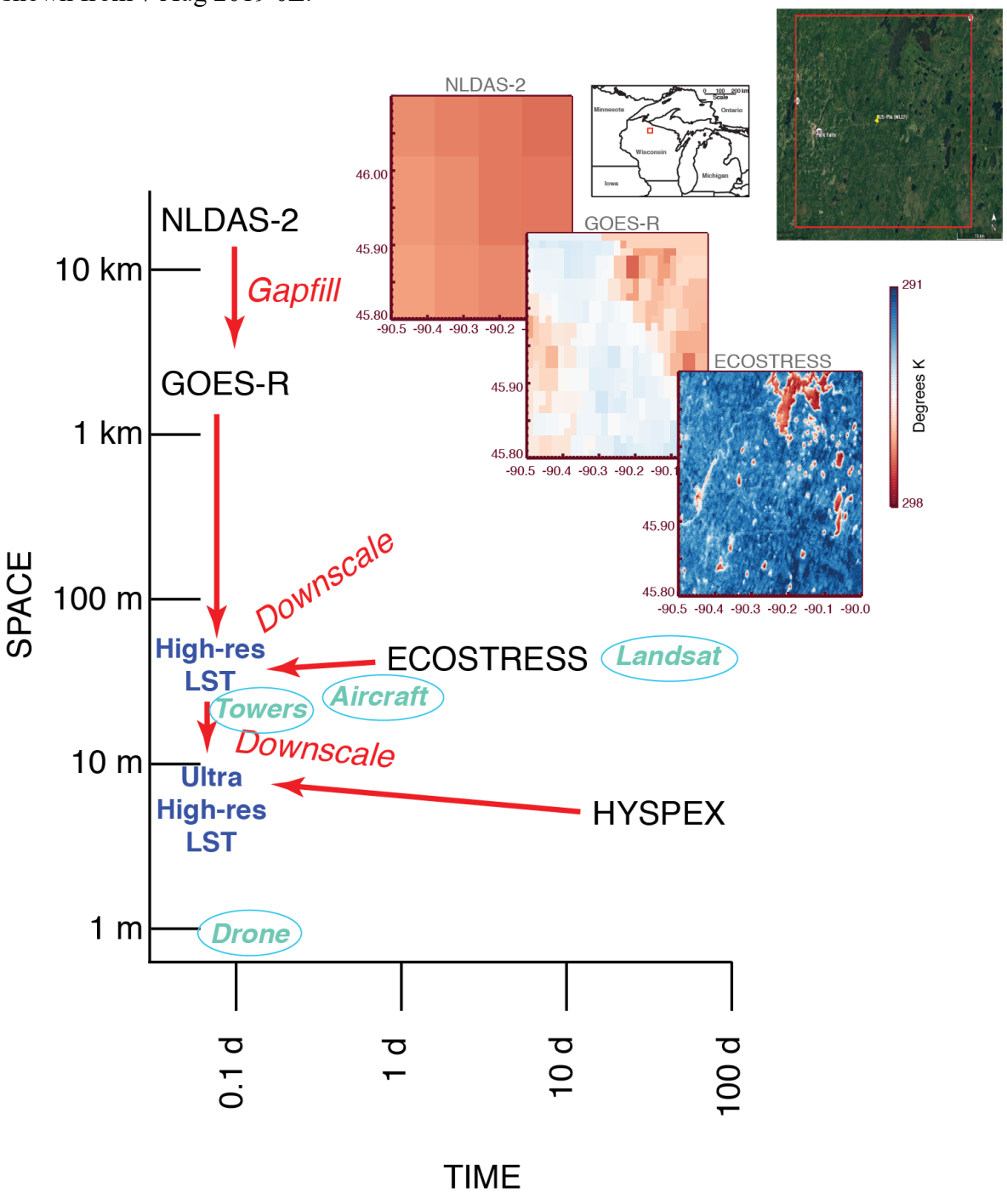

872 **Figure 2.** Strong correspondence of NLDAS-modeled land surface temperature against observed
873 geostationary satellite (GOES) temperature allowed for filling of cloud gaps in GOES with
874 NLDAS.

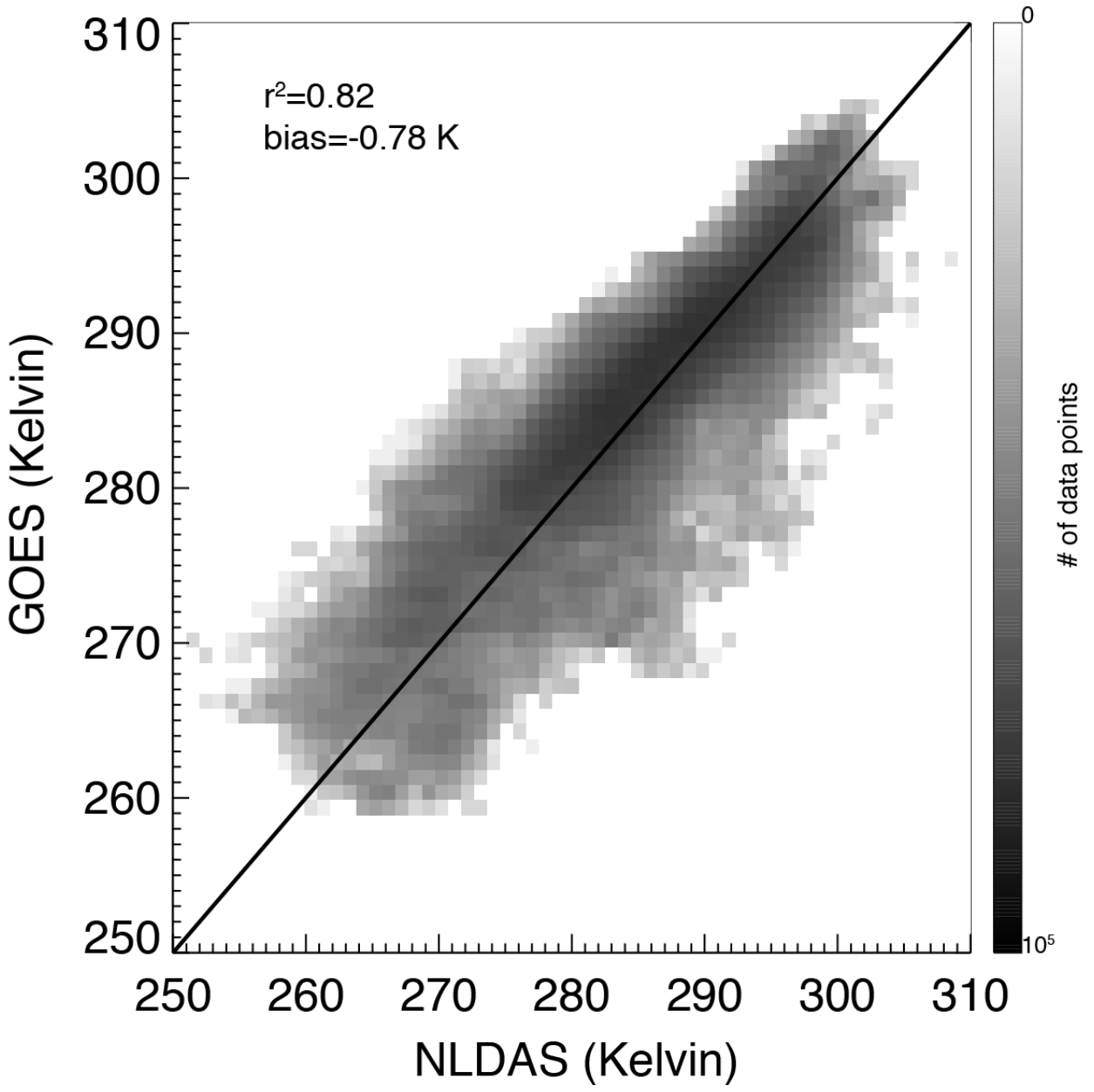

875

Figure 3. Pixel-by-pixel a) linear slope, b) intercept, c) correlation, and d) example regressions for three locations between 25 ECOSTRESS images collected from Jun-Oct 2019 and gap-filled GOES land surface temperature. Pixel-level temporal correlation ranges from 0.59 to 0.95 ($p<0.01$) while individual image spatial correlation ranges from 0.32 to 0.74 ($p<0.001$).

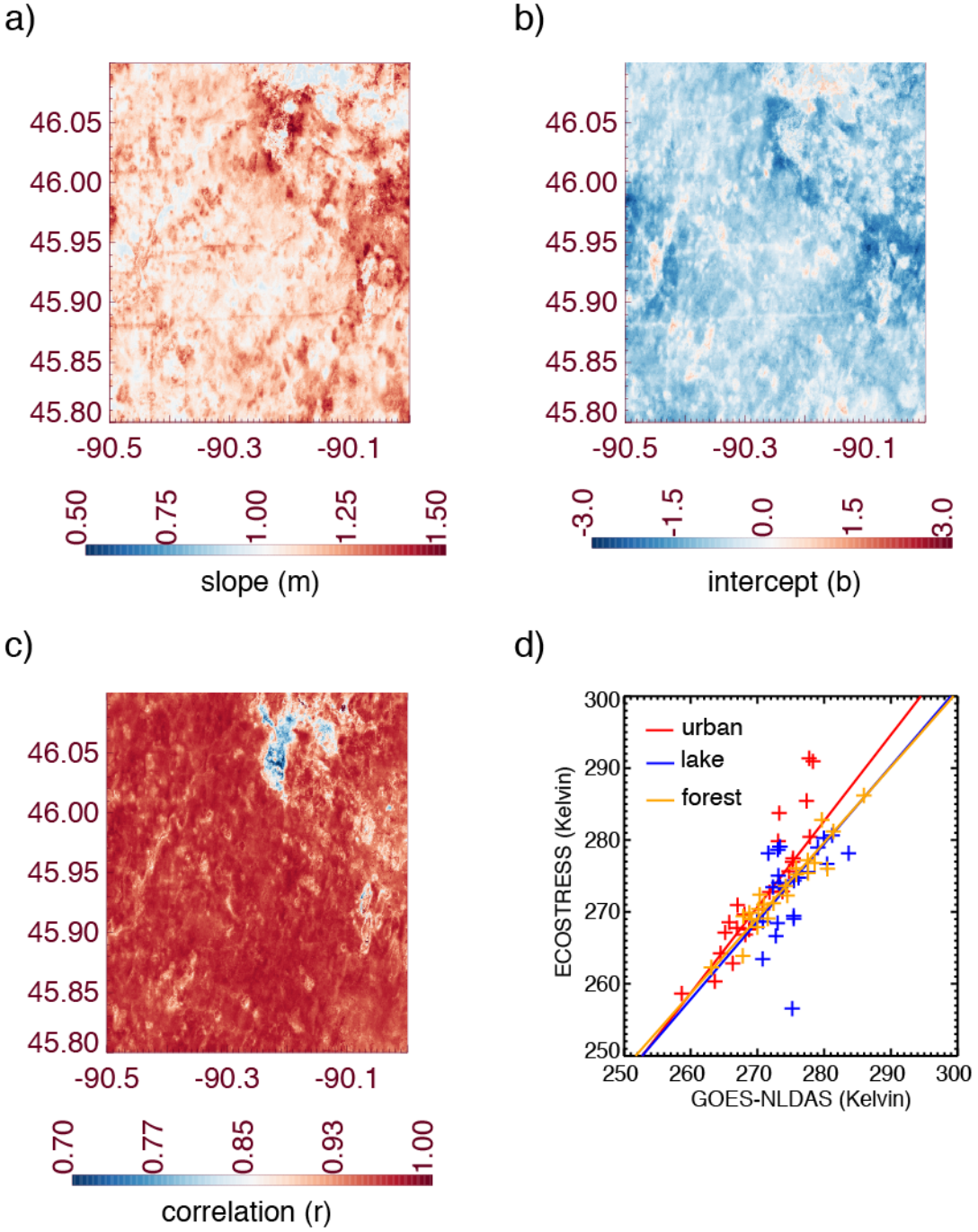

Figure 4. Comparison of land surface temperature diel cycle in a) deciduous forest, b) evergreen forest, c) wetland, and d) lake at four sites within ~2.5 km of each other from tower radiometric observations (orange), NLDAS (black line and gray shading representing spread in three models), GOES (blue crosses, gaps indicate clouds), and the ECOSTRESS fusion product (red line) for mid-July, 2019.

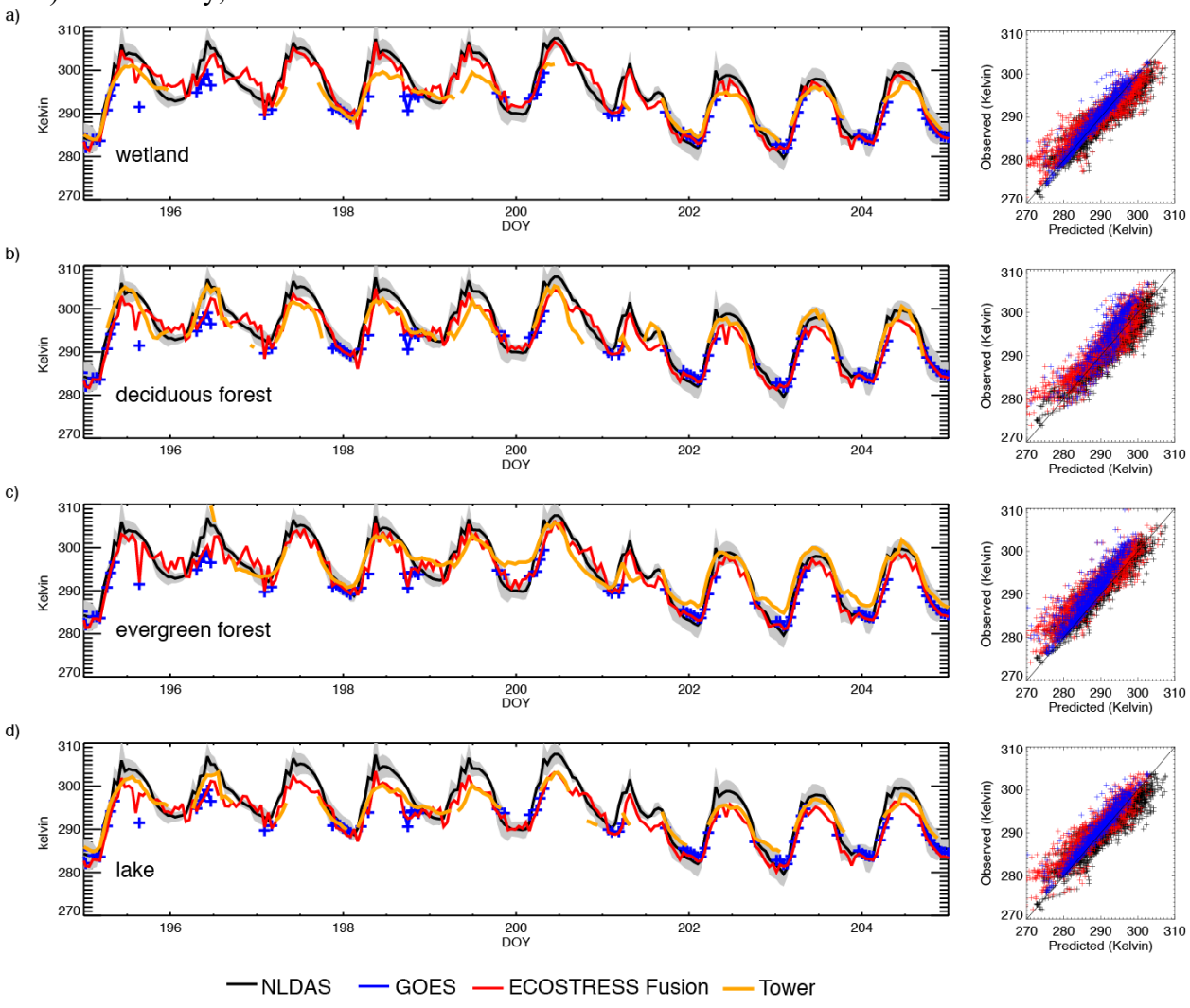

887 **Figure 5.** Comparison of fusion land surface temperature product against upwelling infrared
888 temperature from a) ~10^5 flight LST observations from the University of Wyoming King Air and
889 b) time-series from 17 eddy covariance towers in deciduous forests (green), evergreen forests
890 (brown), and wetlands or lakes (blue).

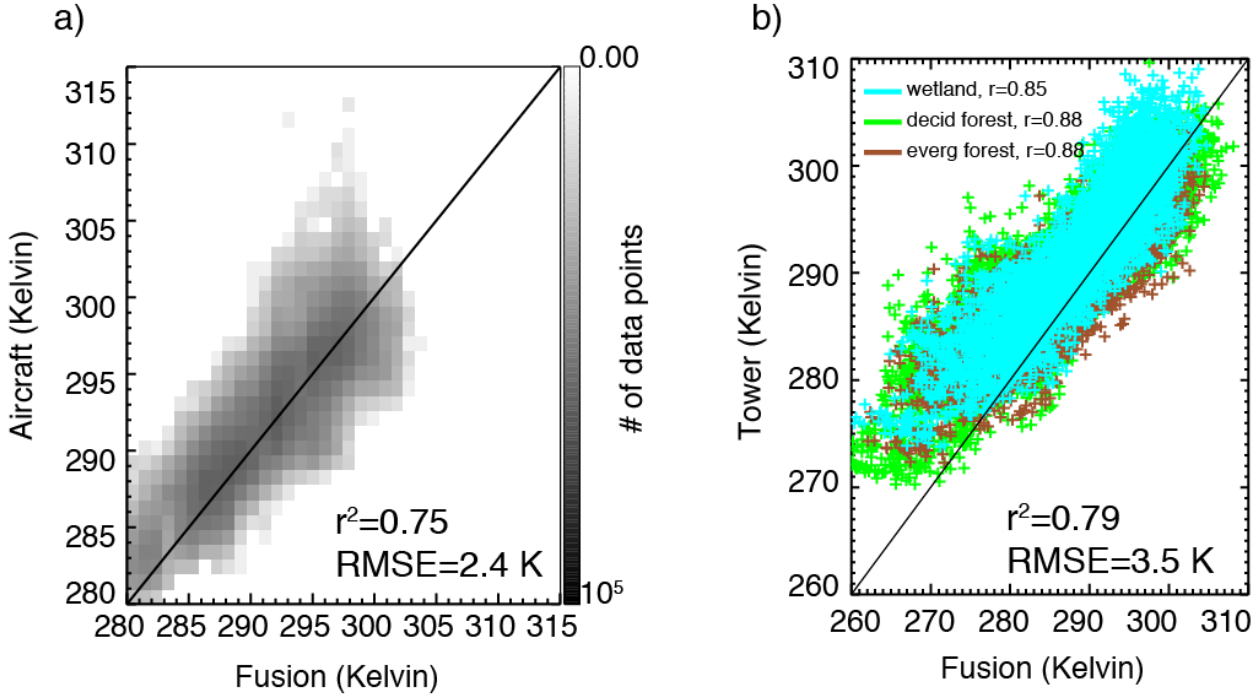

891

892 **Figure 6.** Comparison of a) Landsat two-channel land surface temperature retrieval at 30 m
893 resolution and b) our 50 m fusion product reveals c) relatively good correlation, though warmer
894 areas in Landsat are under-predicted by the fusion.

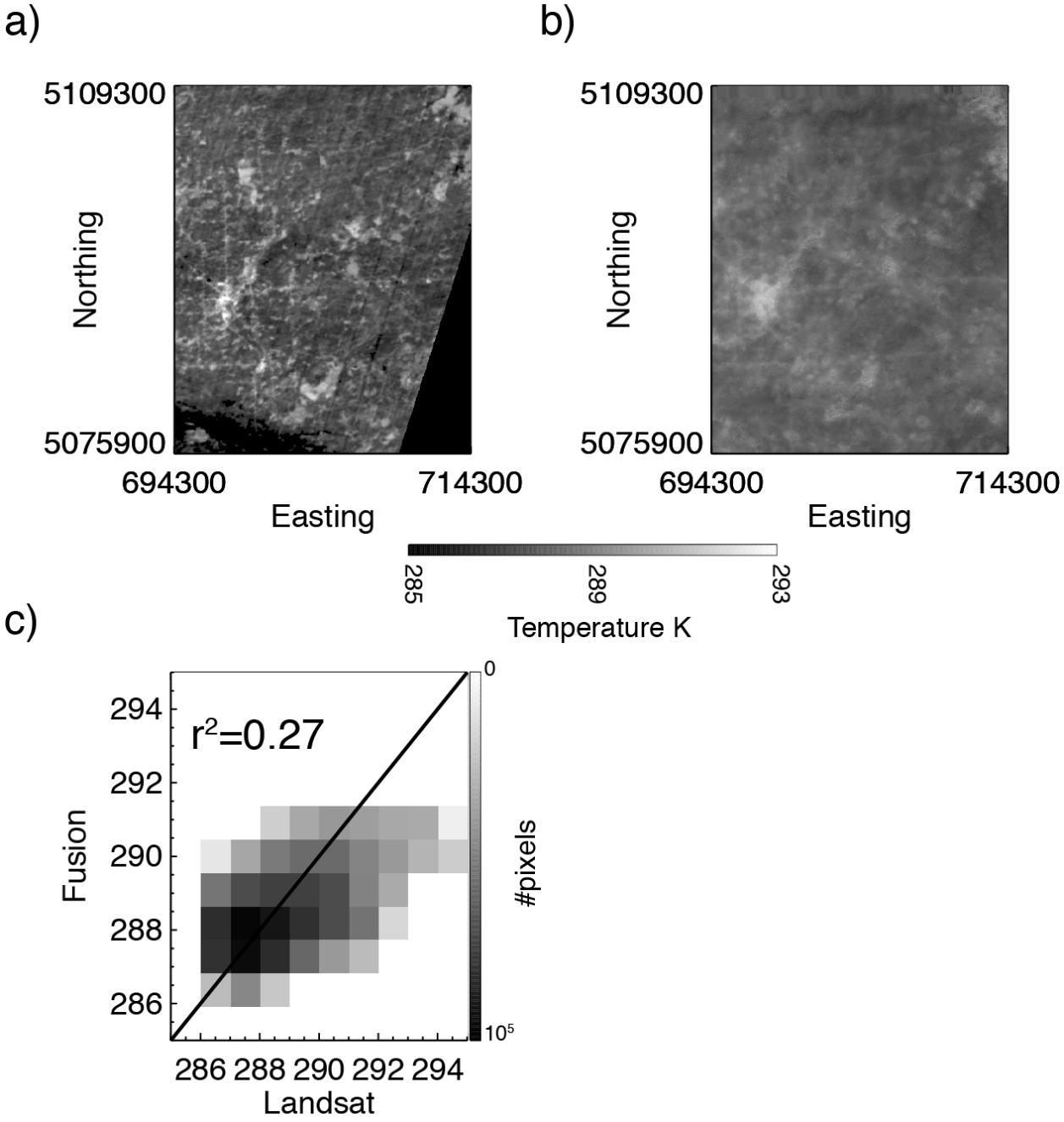

895

Figure 7. Normalized difference spectral index (NDSI) Pearson correlation (r) between band combinations from HySpex airborne hyperspectral imager and drone land surface temperature imagery. The top three most correlated band differences (1470.466 and 1982.657 nm, 709.077 and 760.173 nm, and 504.697 and 651.595 nm, noted in black circles) were used to construct a linear model for downscaling the fusion LST. NDVI region (green square) and PRI region (yellow box) noted for comparison.

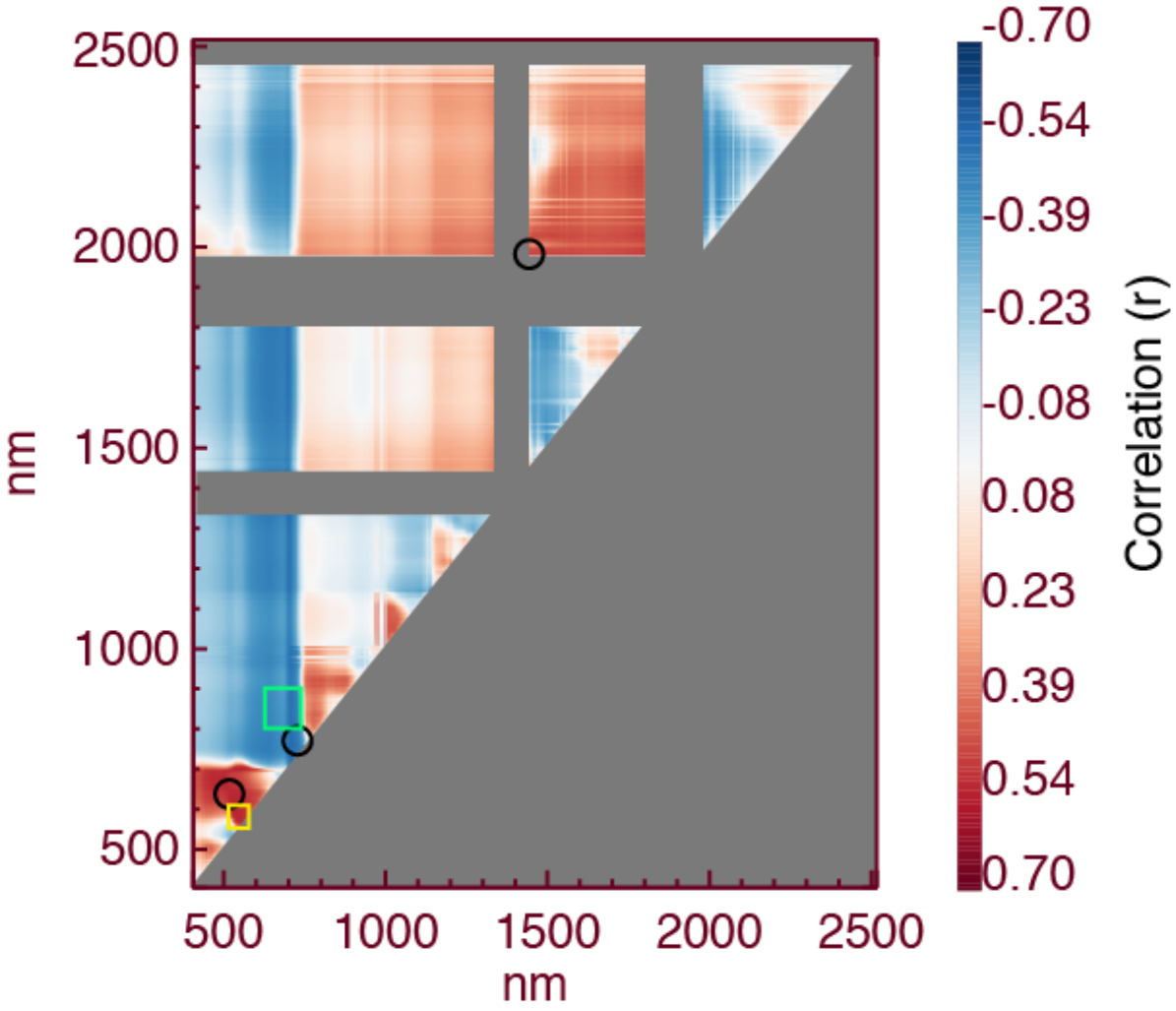

Figure 8. Comparison of a) high-resolution (0.5 m) NOAA UAS drone land surface temperature on 12 July 2019 at 2230Z to b) same image upscaled to 10m, c) original fusion LST product (average of 22 and 23 Z), and d) fusion product further downscaled with visible and near IR hyperspectral imagery collected on 26 June, 13 July, and 6 Aug 2019, demonstrating significant improvement in correlation (r^2=0.14 and RMSE=3.0 K with 50 m and r^2=0.34 and RMSE=1.7 K with 10 m imagery).

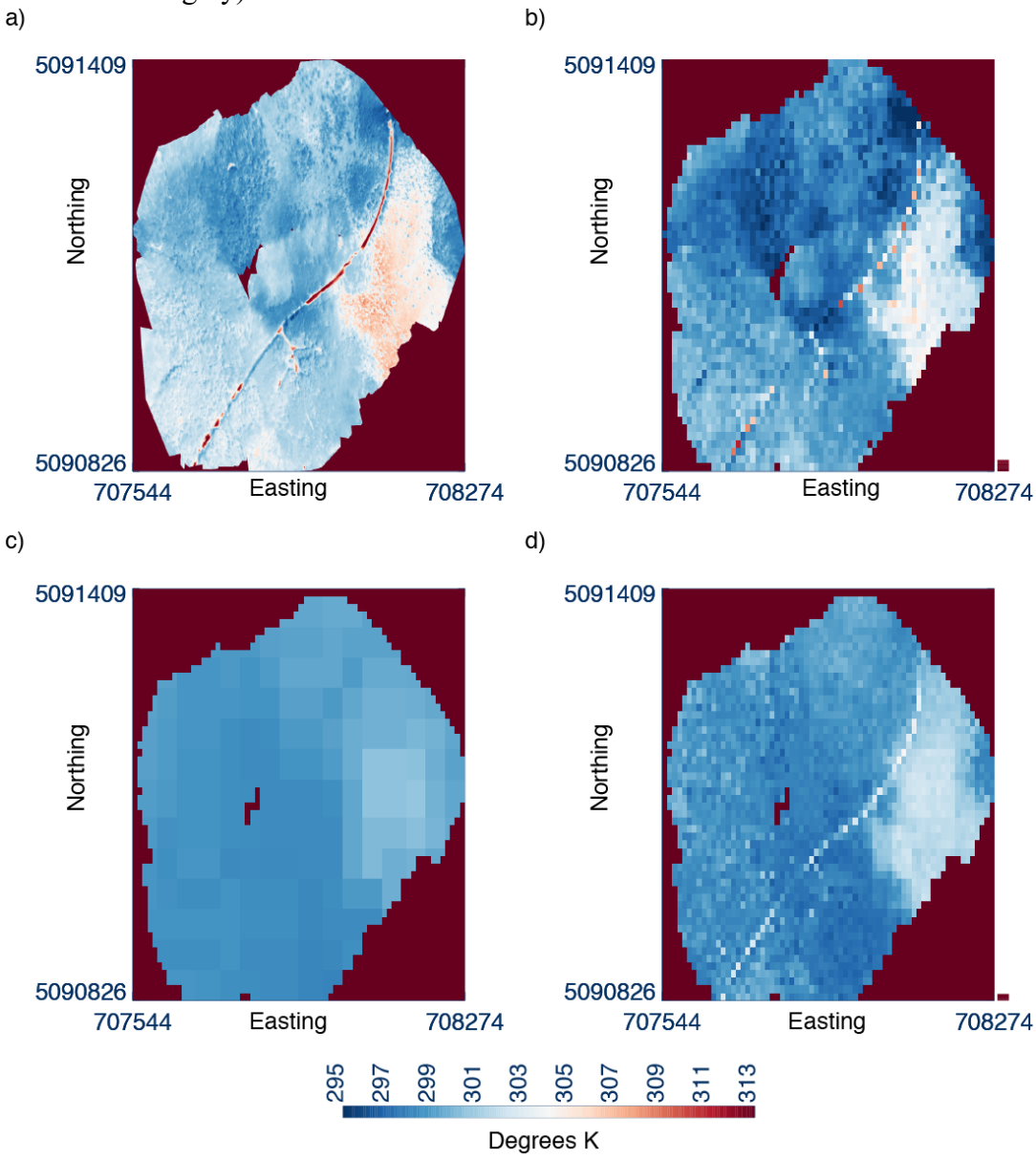

Figure 9. Radially integrated two-dimensional spatial power-spectrum for a single clear-sky day (16 June 2019) compared among a) GOES-NLDAS, b) ECOSTRESS, and c) the fusion land surface temperature product. The fusion product shows better correspondence of spatial autocorrelation and structure to ECOSTRESS than GOES.

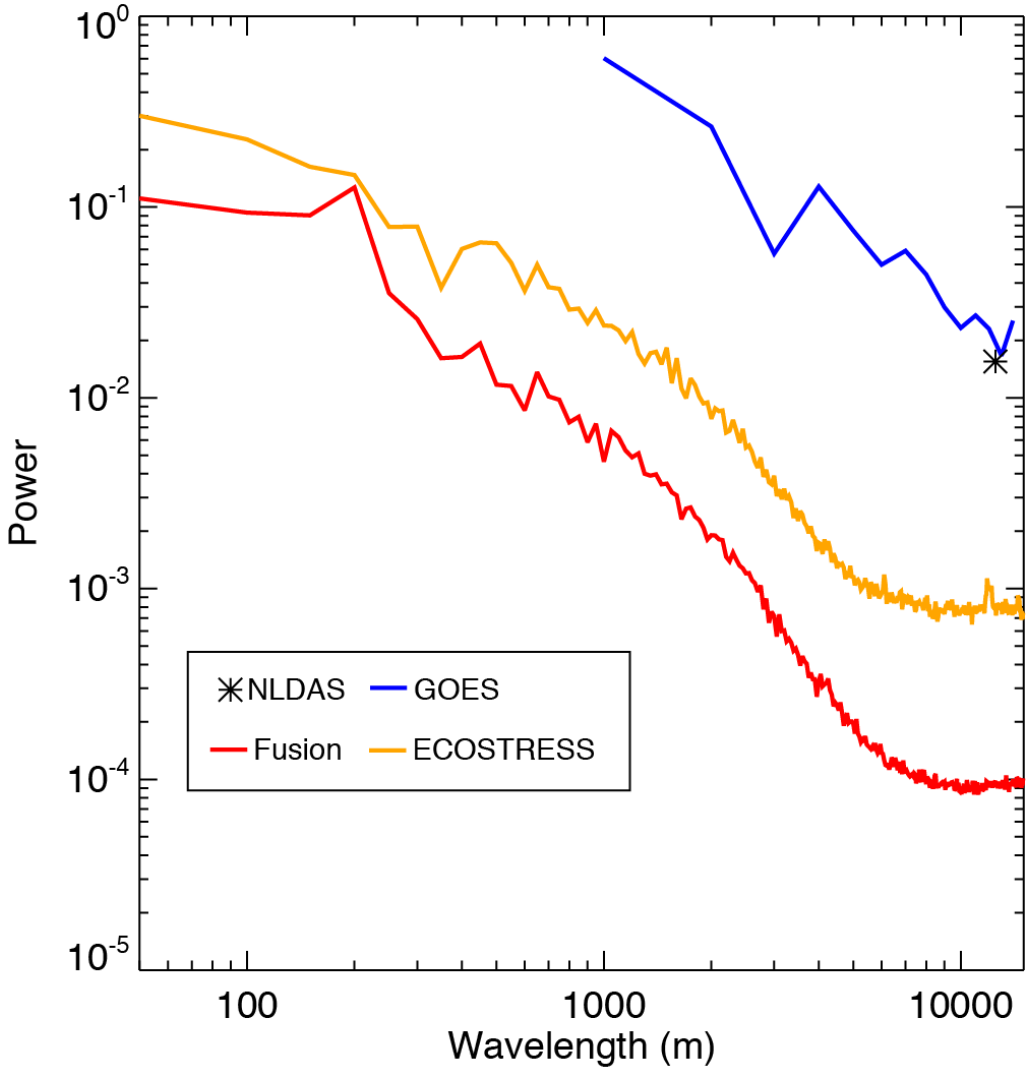

Figure 10. Difference in spatial standard deviation of LST between the 50 m fusion and GOES as a function of hour of day (x-axis) and day of year (y-axis). Increasing heterogeneity in LST is found toward the autumn and afternoons in summer.